

# Entanglement-based quantum information protocols designed with silicon quantum dot platform

Junghee Ryu<sup>1</sup> and Hoon Ryu<sup>1,\*</sup>

<sup>1</sup>Division of National Supercomputing, Korea Institute of Science and Technology Information, Daejeon 34141, Republic of Korea

\*elec1020@kisti.re.kr

## ABSTRACT

Electron spins in silicon quantum dot platform provide great potential for quantum information processing due to excellent physical properties and modern fabrication technologies. Spin-based quantum bit (qubit) operations are intensively studied to realize universal logic gates with a high fidelity, fast gating operations, and basic programmability. Although recent experimental achievements can be considered as remarkable results for utilizing quantum computation, more advanced quantum information protocols should be demonstrated with a large number of qubit system to enable programmability of silicon devices. Here, we computationally explore entanglement-based quantum information protocols in electrically defined five silicon quantum dot system. To this end, device simulations are employed to demonstrate 1-qubit gate and 2-qubit gate operations. Additionally, we discuss the implementations of three applications: the generation of magic states, entanglement swapping, and quantum teleportation in our silicon device. All the results will secure the scalability of quantum information processing with electron spin qubits in silicon quantum dot system.

## Introduction

A gate-driven Silicon (Si) quantum dot (QD) system has been regarded as a promising physical platform for quantum information processing due to its extremely long coherence time<sup>1-4</sup>. Moreover, the Si QD system has outstanding potential to design scalable quantum processors as it can use the state-of-the-art industrial fabrication technologies<sup>5</sup>. Recently, there have been substantial experimental and modeling efforts to understand the physics of electron-spin quantum bits (qubits) in Si QD platforms whose confinement is controlled with magnetic fields and man-made electrodes<sup>6-20</sup>. In particular, elaborated device designs for the realization of universal logic gate operations have been intensively examined. A single qubit rotation can be implemented with a high fidelity larger than 99%<sup>3,4,7,12-18</sup>. Also, it is demonstrated the successful realization of a fast Controlled-NOT (CNOT) gate, which is an essential entangling logic, by using a single microwave pulse in double QD (DQD) platform and the single-step CNOT logic is completed in  $\sim 200$  ns<sup>6</sup>, which are significant results compared to the other physical platforms<sup>6</sup>.

Experimentally feasible qubits operations can provide frameworks for constructing programmable quantum processors. It is explored the programmability of the two-qubit quantum processor in a Si DQD system by implementing the well-known quantum algorithms; the Deutsch-Josza algorithm and the Grover algorithm<sup>19</sup>. Recently, remarkable experimental results for multi-qubits have been continuously reported. A generation of three-qubit Greenberger-Horne-Zeilinger (GHZ) entangled state defined in Si triple quantum dot (TQD) system is studied<sup>7</sup> and quantum error correction is investigated in Si TQD<sup>20</sup>. A six-qubit quantum processor in Si platform is studied experimentally and the creation of the three-qubit GHZ entanglement is tested by the six-qubit processor<sup>8</sup>. Although all the results open a new way of computation for electrons spin-qubit in Si QDs platform, device designs and control engineering of a large number of QDs are still critical issues that must be uncovered with modeling to secure the scalability of quantum information processing.

In this paper, we extend the modeling approach used in<sup>9-11</sup> to the five QD (FQD) structure in Si and examine electrostatic control engineering to realize the programmable Si-based quantum processor. To this end, our in-house code package can be used for full-scale device simulations of the initializations and time-dependent behaviors of the electron spin-qubit in Si FQD system, where implementing the single qubit controls and two qubits entangling logic gate are the baseline for the investigation. Although the Si QD platform can implement the single-step CNOT gating operation, it is shown that the single-step CNOT logic is fragile against the charge noises which are omnipresent in semiconductor devices<sup>10</sup>. Instead, in our simulation we conduct a multi-step CNOT gate operation consisting of two single qubit rotations and one controlled-Z gate, which is more feasible experimentally as it can be implemented only with the DC field generated from the micromagnet. Combining these results allow us to implement three well-known quantum information applications; the creation of the magic states, the entanglement swapping protocol, and the quantum teleportation.

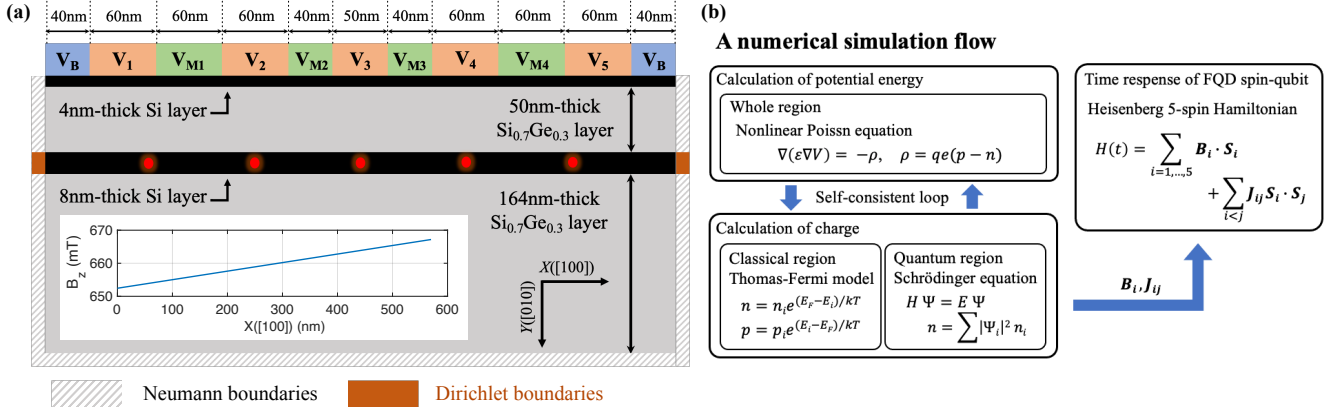


**Figure 1.** Simulation domain of the silicon-based five quantum dot (Si FQD) system and modeling approach. (a) A 2D simulation domain representing a Si FQD system that is assumed to be infinitely long along the Z ([001])-direction. In the middle 8nm-thick Si layer, the linear five-QD array can be created by controlling the eleven gate biases (the two barrier gates denoted as  $V_B$  are set to 200 mV). A spatial distribution of the static magnetic field  $B_z$  is given in the inset. (b) A numerical simulation flow. Spatial distributions of charge and potential are calculated with the self-consistent loop of the device simulations based on the bulk physics and the empirical representation of electronic structures. The results from the loop are used to investigate the time responses of FQD spin-qubit system.

## Methods

A 2D simulation domain for the Si FQD system shown in Fig. 1(a) is extended from the structure we previously constructed to describe the Si double QD system<sup>11</sup>. The target platform of modeling in this work is formed by a silicon and silicon-germanium (Si/SiGe) heterostructure that consists of 4nm-thick Si layer, 50nm-thick SiGe layer, 8nm-thick Si layer, and 164nm-thick SiGe layer from top to bottom in the Y ([010])-direction. The fractions of Si and Ge in SiGe layers are 70% and 30%, respectively. Then, a quantum confinement in the Y ([010])-direction is formed in the middle 8nm-thick Si layer because of the Si and SiGe conduction band offset. Moreover, applying appropriate DC gate biases from the top electrodes can create a lateral confinement along X ([100])-direction in the 8nm Si layer. As our target system is the five quantum dots, the top electrodes are composed of two barrier gate biases ( $V_B$ ), five gate biases ( $V_1, \dots, V_5$ ) for each QD, and four middle gate biases ( $V_{M1}, \dots, V_{M4}$ ) between QDs, in which the five potential valleys are formed. In particular, the five gate biases  $V_i$  control the energies of the electron in each QD and the four middle biases control the barrier heights between the nearest-neighbor QDs. Changing the barrier heights affect the exchange interaction ( $J$ ) between the nearest-neighbor QDs, thus the value  $J$  plays a control factor to generate the quantum entanglement. A static magnetic field  $B_z$  is applied with a gradient along the X ([100])-direction to make the Zeeman splitting energies of electron ground states distinguishable because the differences of the Zeeman splittings depend on the strength of the magnetic field  $B_z$  and it is because the linear FQD are spatially separated along the X ([100])-direction. Thus, it is possible to address each qubit individually, which enable us to implement single qubit gate operations.

We employ a self-consistent process of the device simulations to calculate the electrostatic profiles of the FQD system as shown in Fig. 1(b), in which we can obtain the spatical distribution of potential energy and electron density of our FQD system. We use a nonlinear Poisson formula to calculate the potential profile, whereas we need to employ two methods to evaluate the charge distribution depending on the regions where the different physical theories are governed. As most of the electrons are expected to confine in the middle Si layer in Fig. 1(a), the region should be calculated quantum mechanically. On the other hand, the region of SiGe layers is assumed to have no charges at very low temperature which can be treated in a classical physics, so that the charge profile in this region is solved with the physics of bulk semiconductors. Once the charge profile is determined in two ways, the nonlinear Poisson solver is calculate in the entire region to update the potential energy profile. Such an iterative process continues until the newly obtained potential profile satisfies the convergence criterion of  $10^{-10}$  eV. When we obtain the electrostatic profiles of the ground states for the FQD system involving the Zeeman-splitting energies and exchange interactions, we can construct the Heisenberg 5-spin Hamiltonian with the outcomes, and 5-qubit time responses of the FQD system can be then calculated.

## Results and Discussion

Initializing the spin-qubit states of our target FQD system is the first step for implementing logic gate operations. We use the electron down-spin ( $|\downarrow\rangle$ ) and up-spin ( $|\uparrow\rangle$ ) ground states of the FQD to encode the qubit states  $|0\rangle$  and  $|1\rangle$ , respectively. As

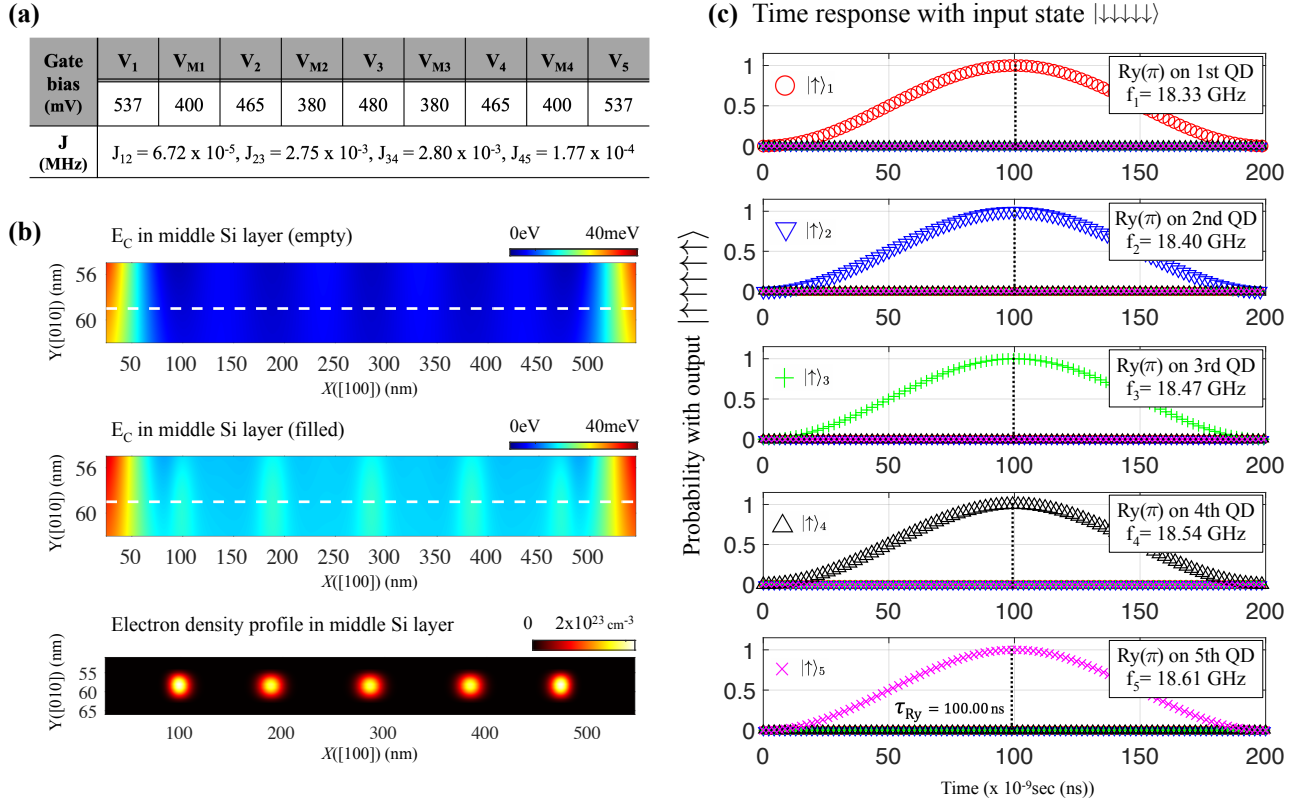


**Figure 2.** Initialization of the linear FQD system. (a) Gate biases for the initialization and the exchange interaction  $J$  between the nearest-neighbor QDs. The leftmost and rightmost barrier gates  $V_B$  are set to 200 mV. The range of  $J$  obtained from the simulation is several kHz or lower, which is definitely at the weak-interactions. (b) The first two subfigures show the potential profile in the middle Si layer when the QDs are empty and all the QDs are filled with one electron, respectively. The last one shows the electron density profile in the middle Si layer when each QD contains a single electron, i.e., it is initialized. (c) Five-qubit time responses of our FQD system under an AC magnetic field whose driving frequency is set equal to the Zeeman splitting energies, respectively. The electron spin-qubit in each QD can be manipulated in the regime of a weak exchange interaction.

mentioned previously in the Methods, applying appropriate DC biases can create the five potential valleys and the bias conditions need to be elaborately designed to ensure that a single electron can occupy the down-spin ( $|\downarrow\rangle$ ) ground state in each QD. The desired bias conditions obtained by our device simulation are shown in Fig. 2(a), which lead to the initialization of all confined electrons into the down-spin state  $|\downarrow\downarrow\downarrow\downarrow\downarrow\rangle$ , where we omit the tensor product symbol ( $\otimes$ ) between the states. For given bias conditions, the potential shapes of the FQD system become almost identical that is known as the symmetric-biasing condition, as shown in the second subfigure of Fig. 2(b). The subfigures in Fig. 2(b) ensure that only one electron is confined in each QD with the obtained basis conditions. More precisely, the first two subfigures in Fig. 2(b) show the spatial distribution of the conduction band minimum energy ( $E_C$ ) in the middle 8nm Si layer that is represented with respect to the energetic position of the Fermi energy ( $E_F$ ) for the empty and initialized (each QD is occupied with one electron) cases, respectively. The subfigure in bottom of Fig. 2(b) presents the electron density profile when each QD is filled with one electron. When initialized, the five Zeeman-splitting energies denoted as  $E_{Z_i}$  for  $i$ th QD are calculated as  $(E_{Z_1}, E_{Z_2}, E_{Z_3}, E_{Z_4}, E_{Z_5}) = (18.33, 18.40, 18.47, 18.54, 18.61)$  GHz and the exchange interaction  $J_{ij}$  between  $i$ th and  $j$ th QDs becomes  $(J_{12}, J_{23}, J_{34}, J_{45}) = (0.067, 2.747, 2.795, 0.177)$  kHz. Since the interactions  $J_{ij}$  are quite small in the order of kHz compared to the case of double QD system ( $\sim 75$  kHz at the weak-interaction mode<sup>11</sup>), all the spin-qubit can be individually addressed upon initialization. Note that we here consider the  $J_{ij}$  only for the nearest-neighbor QDs.

Now we are ready to implement the individual gate operation on each qubit. The implementations of single- and two-qubit gates are necessary operations for universal quantum computing. The Zeeman-splitting energies  $E_{Z_i}$  and the exchange interaction  $J_{ij}$  obtained above can be used to construct the Heisenberg five-spin Hamiltonian and the time responses of the qubits can be calculated by solving a time-dependent Schrödinger equation with the spin Hamiltonian. In our simulation, we

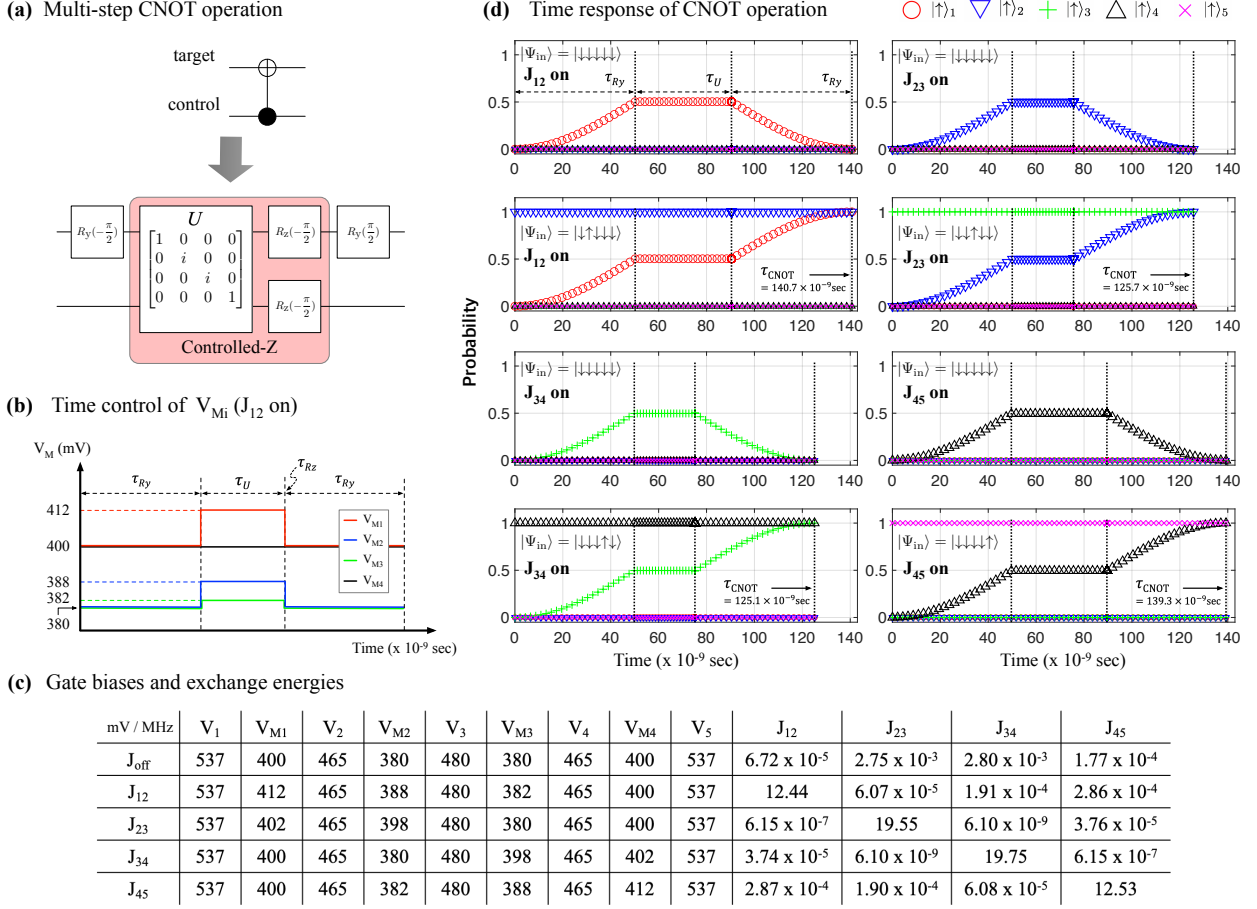


**Figure 3.** Multi-step CNOT gate operation with DC entangling logic. (a) The CNOT logic can be implemented by using three steps consisting of two 1-qubit rotations  $R_y(\pm\pi/2)$  and a controlled-Z (CZ) gate. Additionally, the CZ gate can be conducted with a 2-qubit unitary  $U$  and two 1-qubit rotation  $R_z(-\pi/2)$  that can be performed by only DC biases. As explained in the main text, adjusting a single middle gate bias is insufficient to increase the target exchange interaction. (b) We show that the time control of  $V_{Mi}$  for the strong interaction  $J_{12}$ . The  $V_{M1}$ ,  $V_{M2}$ , and  $V_{M3}$  are increased simultaneously to implement the  $U$  gate, while  $V_{M4}$  remains unchanged. Here, we assume that the  $R_z$  operation is completed instantaneously. (c) Gate biases and exchange interactions calculated with our device simulation are summarized. (d) The real-time responses of the multi-step CNOT logic operations. When the control spin-qubit state is in  $|\uparrow\rangle$ , the target state is flipped from  $|\downarrow\rangle$  to  $|\uparrow\rangle$ .

conduct a  $R_y(\pi)$  operation that is a one-qubit rotation by  $\pi$  radian phase around the Y-axis. A time-varying magnetic field  $B_y(t) = B_o \cos(\omega_D t + \theta)$  is applied along the Y ([010])-direction, and it is incorporated in the Heisenberg Hamiltonian. As the inhomogeneous  $B_z$  makes the Zeeman-splitting energies  $E_{Zi}$  distinguishable, in the regime of weak interaction the  $R_y(\pi)$  can be individually implemented by setting the driving frequency  $\omega_D$  of the magnetic field to  $E_{Zi}$ . For instance, when the drive frequency is set to 18.33 GHz (the Zeeman splitting of the 1st QD), the electron spin resonance occurs only in the 1st QD and the spin-qubit in the rest QDs remains unchanged. Figure 2(c) shows the simulation results of the five-qubit time responses with the input state  $|\downarrow\downarrow\downarrow\downarrow\downarrow\rangle$ , where the gating operations are completed in (100.11 ns, 100.02 ns, 99.92 ns, 99.80 ns, 99.72 ns) with the fidelities about 99.99% for each QD, respectively.

To implement two-qubit entangling logic gate, the exchange interaction need to be strong enough such that the resonant frequency of one spin-qubit state is dependent on the other state. That is, the individual manipulation of the qubit state is no longer valid. Instead, the conditional two-qubit gating operation can be realized by selecting the corresponding resonant driving frequency. In a silicon QD platform, it is possible to implement the single-step CNOT gate operation which is driven with a single control pulse<sup>6</sup>. Its gating time is fast ( $\sim 200$  ns) compared with the other physical platforms. However, recently it is shown that the single-step CNOT logic is not robust to the charge noises which are omnipresent in silicon device<sup>10</sup>. Our target example of the entangling gate is the multi-step CNOT logic as shown in Fig. 3(a). In our linear array of FQD system, we

consider the spin-qubit on the left (right) QD from the selected nearest-neighbor QDs as the target (control) qubit. In the circuit representation, the upper (lower) layer qubit is regarded as the target (control) qubit.

The multi-step CNOT operation can be implemented by applying a sequence of a  $R_y(-\pi/2)$ , a controlled-Z (CZ), and a  $R_y(\pi/2)$  as shown in Fig. 3(a). The two  $R_y$  operations conducted with target qubits should be carried in the weak interaction. On the other hand, the CZ gate can generate the two-qubit entanglement, thus the operation must be implemented in the regime of a strong interaction. Furthermore, the CZ gate can be decomposed into a single Ising ZZ gate with the phase  $\pi/2$  and two  $R_z$  rotations that are native gates to the Si QD platform<sup>10</sup>. As explained previously, the exchange interaction  $J$  can be enhanced by increasing the middle gate bias  $V_M$  as it lowers the barrier height between two QDs. However, unlike the DQD and TQD cases<sup>9-11</sup>, increasing only the single middle gate between two QDs is not sufficient to obtain the desired strong exchange interaction for implementing the CNOT logic. The other middle gate biases also should be controlled. Figure 3(b) shows the time behavior of the middle gate biases to increase the interaction  $J_{12}$ , where the voltages of the middle biases ( $V_{M1}, V_{M2}, V_{M3}, V_{M4}$ ) are changed as (400, 380, 380, 400) mV  $\rightarrow$  (412, 388, 382, 400) mV. Note that the  $V_{M1}, V_{M2}, V_{M3}$  increase, while  $V_{M4}$  remains unchanged. With the gate biases, the exchange interaction  $J_{12}$  becomes 12.44 MHz which is reasonable to the results reported experimentally<sup>7,8</sup>. In our device simulation, we obtain the gate biases at the regime of weak and strong interactions and calculate corresponding the  $J_{ij}$ , which are summarized in Fig. 3(c). To test the validity of our simulation results, the real-time responses of the multi-step CNOT are conducted with appropriate input spin qubits, as shown in Fig. 3(d). For example, in case of the exchange interaction  $J_{12}$  on, the target spin-qubit (red) of the 1st QD can be flipped as  $|\downarrow\rangle_1 \rightarrow |\uparrow\rangle_1$  only when the control spin-qubit of the 2nd QD is in  $|\uparrow\rangle_2$  (blue), which yields the CNOT logic for QD1 and QD2. It applies to the other cases, where one can see the conditional flip operations. Note that the CNOT operations for 1-2 QDs and 4-5 QDs are completed in (140.7 ns) and (139.3 ns), and the CNOT for 2-3 QDs and 3-4 QDs are completed in (125.7 ns) and (125.1 ns), respectively. This is because the exchange energies for ( $J_{23}, J_{34}$ ) are higher than the one for ( $J_{12}, J_{45}$ ) as follows: ( $J_{12}, J_{45}$ ) = (12.44, 12.53) MHz and ( $J_{23}, J_{34}$ ) = (19.55, 19.75) MHz. The gate fidelity in each case is almost reached to 99.99%.

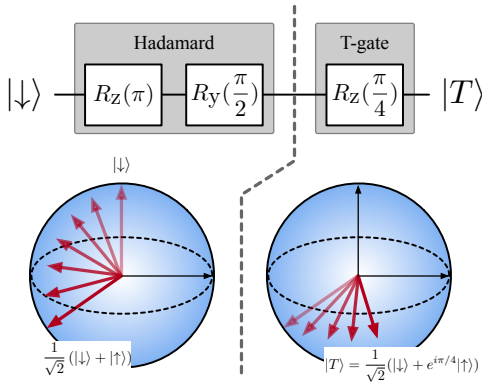
To demonstrate the programmability of our FQD system, we will explore three examples of quantum information applications: (1) the magic state generation, (2) entanglement swapping protocol, and (3) quantum teleportation. For each case, we design the quantum circuits to implement the above applications on the FQD platform and analyze the gate operations and the corresponding output states.

Let us first investigate the generation of the magic state. It is well known that the magic state plays a crucial role for the realization of the fault-tolerant quantum computing<sup>21</sup>. We here consider a  $N$ -qubit magic state without entanglement, each of which is in a form of  $(|\downarrow\rangle + e^{i\pi/4}|\uparrow\rangle)/\sqrt{2}$ . The single qubit magic state can be obtained by applying the Hadamard gate and the  $T$ -gate on the state  $|\downarrow\rangle$ <sup>22</sup>. The  $T$ -gate is known as  $\pi/4$  phase rotation gate about  $Z$ -axis (up to global phase), which is given by  $|\downarrow\rangle \langle\downarrow| + e^{i\pi/4}|\uparrow\rangle \langle\uparrow|$ . As the gate operation of the single qubit is enough to produce the magic state, the middle gate biases do not need to be controlled to increase the exchange interactions  $J_{ij}$ . Instead, all gate operations can be conducted in the case of the weak interaction. As shown in Fig. 4(a), we conduct the  $R_z(\pi)$  and  $R_y(\pi/2)$  sequentially for simulating the Hadamard gate and the  $R_z(\pi/4)$  operation for the  $T$ -gate. Figures 4(b)-(d) show the real and imaginary part of the density matrices of the  $N$ -qubit magic states, respectively. The 1-qubit is prepared in the leftmost QD in our linear FQD system. The 3-qubit case (Fig. 4(c)) is generated by applying the logic gates to three (1st-to-3rd) qubits, and the 5-qubit case (Fig. 4(d)) is the result where the qubit operations are conducted to all the five qubits. Even in the case that single qubit operations are conducted to every spin-qubit, individual qubit addressing works well in our FQD system and  $N$ -qubit magic states are generated as intended. This is because the  $R_z(\pi/4)$  gate operation can be easily operated with only DC pulses.

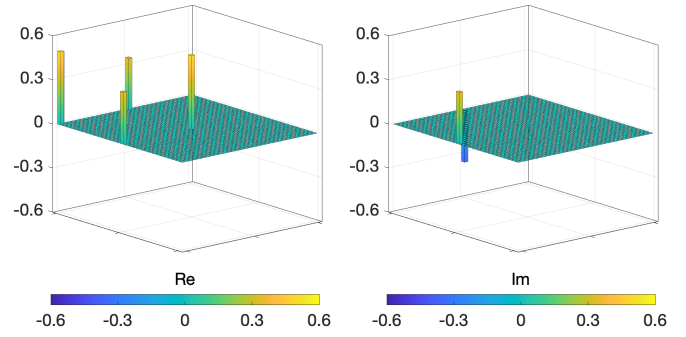
The next applications we explore are the entanglement-based applications such as the entanglement swapping protocol and the quantum teleportation. The entanglement swapping are used to prepare remote quantum entanglement between subsystems that have never been interacted. Thus, it is regarded as a key ingredient to realize the long-distance quantum communication<sup>23-25</sup>. Quantum teleportation offers a new way of sending quantum information. Due to the no-cloning theorem of the quantum state, the quantum information cannot be copied and pasted similar to the classical method. In the quantum teleportation process, the quantum entanglement is a necessary resource as a quantum channel to beat the classical method. Therefore, in our FQD system, we first implement the entanglement swapping protocol to produce the remote quantum entanglement and deploy the entanglement as the quantum channel of the quantum teleportation.

Let us begin by exploring the entanglement swapping protocol. The first step of the protocol is to prepare the two independent Bell pairs for (QD1, QD2) and (QD3, QD4), respectively. In our simulation, the two Bell pairs can be written by  $|\Phi^+\rangle_{12} \otimes |\Phi^+\rangle_{34}$ , each of which is given by  $|\Phi^+\rangle_{ij} = (|\downarrow\downarrow\rangle_{ij} + |\uparrow\uparrow\rangle_{ij})/\sqrt{2}$ . To this end, first applying the Hadamard gates on the QD2 and QD4 simultaneously can create an equal superposition state for the spin-up and spin-down qubits. Then, we utilize the multi-step CNOT operations to (QD1, QD2) and (QD3, QD4), respectively, to create the entanglement, where we employ the 2nd and 4th QDs spin qubits as the control qubits. As the entangling logics can be conducted at the regime of strong interaction  $J$ , the appropriate middle gate biases need to be controlled by the parameters in Fig. 3(c). Then, the output state in the stage (i) in Fig. 5(a) is prepared in the tensor product of the two Bell pairs as  $|\Phi\rangle_{12} \otimes |\Phi\rangle_{34}$ . Figure 5(b) show the density

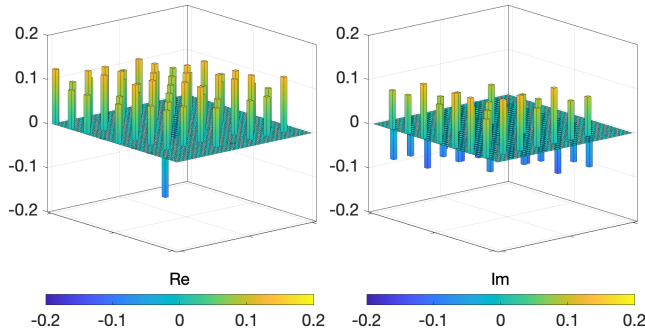
(a) Quantum circuit for magic state



(b) 1-qubit magic state



(c) 3-qubit magic state



(d) 5-qubit magic state

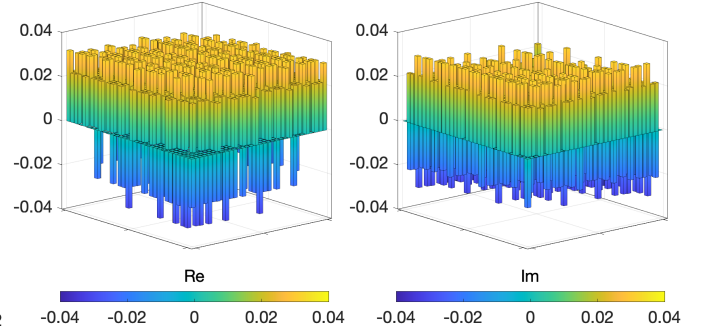


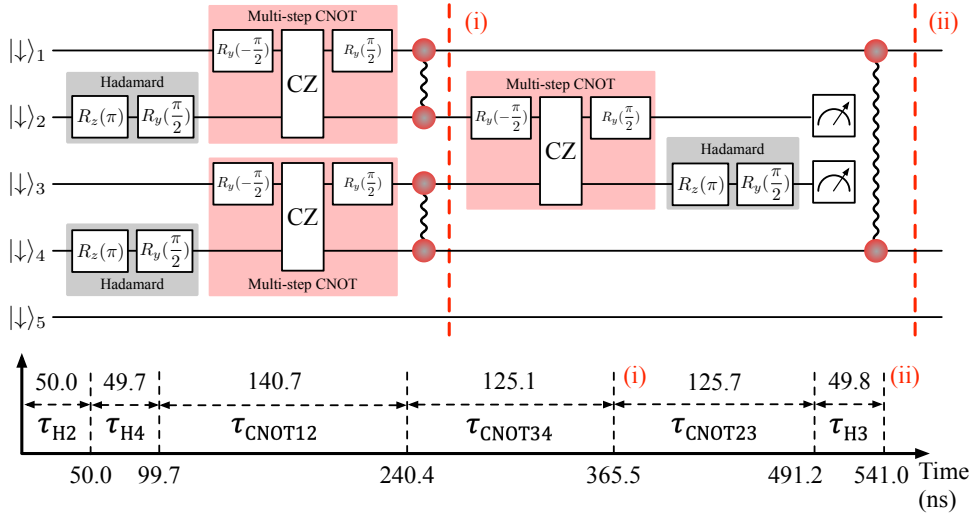
**Figure 4.** The  $N$ -qubit magic state. (a) Quantum circuit to generate a magic state. Our working example of the magic state can be prepared by applying the Hadamard and  $T$ -gate operations sequentially on the state of  $|\downarrow\rangle$ . In our simulation, the Hadamard gate is conducted by applying  $R_z(\pi)$  and  $R_y(\pi/2)$  and the  $T$ -gate by  $R_z(\pi/4)$ . (b) An one-qubit magic state is prepared by applying these gate operations sequentially to the 1st qubit (leftmost QD in our FQD system). The left and right subfigures show the real and imaginary parts of the density matrix, respectively. (c) The density matrix of three-qubit magic state (1st, 2nd and 3rd qubit) and (d) that of five-qubit magic state.

matrix of the output state and it exhibits sixteen peaks of the real part with the values about 0.25, which is clearly expected for the tensor product of the Bell pairs. The state fidelity of the output state is reached to 99.99%. The lower figure of Fig. 5(a) shows the operating time for each logic gate. The circuit of preparing the two Bell pairs is completed in 365.5 ns.

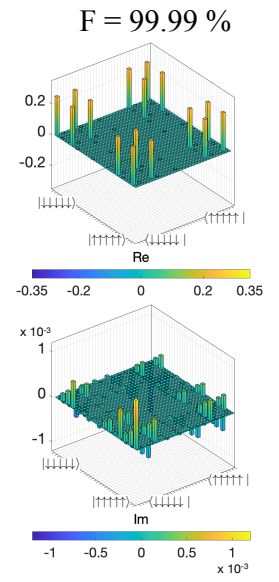
The next step is to conduct the Bell measurement on the spin-qubit of QD2 and QD3. Although the Bell measurement is an entanglement basis measurement, it can be realized by the computational basis (here the spin-up and -down qubit bases) with help of additional entangling operation. To this end, we apply the multi-step CNOT to the QD4 and QD5, followed by the Hadamard gate on QD5. It can map the four Bell bases into the four two-qubit spin states ( $|\downarrow\downarrow\rangle$ ,  $|\downarrow\uparrow\rangle$ ,  $|\uparrow\downarrow\rangle$ ,  $|\uparrow\uparrow\rangle$ ). Depending on the outcomes of the measurements on the QD2 and QD3, the output spin qubits for QD1 and QD4 can be converted to one of four Bell entangled states. In our simulation, the measurement process is simulated by employing the projection operator corresponding to the desired outcome basis. For our case, we employ the following four projectors:  $\mathbf{1} \otimes |\downarrow\rangle\langle\downarrow| \otimes |\downarrow\rangle\langle\downarrow| \otimes \mathbf{1} \otimes \mathbf{1}$ ,  $\mathbf{1} \otimes |\downarrow\rangle\langle\downarrow| \otimes |\uparrow\rangle\langle\uparrow| \otimes \mathbf{1} \otimes \mathbf{1}$ ,  $\mathbf{1} \otimes |\uparrow\rangle\langle\uparrow| \otimes |\downarrow\rangle\langle\downarrow| \otimes \mathbf{1} \otimes \mathbf{1}$ , and  $\mathbf{1} \otimes |\uparrow\rangle\langle\uparrow| \otimes |\uparrow\rangle\langle\uparrow| \otimes \mathbf{1} \otimes \mathbf{1}$ . Corresponding output entangled states are shown in Fig. 5(c). The original output state are calculated with the five-spin qubit states as shown in the left density matrix in the red box of Fig 5(c), but for the sake of simplicity, we pick out the nonzero components from the full density matrix as described in the right density matrix in the red box of Fig 5(c), which represent the components of the two-qubit entangled states. For each measurement outcomes for the QD2 and QD3 as  $|\downarrow\downarrow\rangle_{23}$ ,  $|\downarrow\uparrow\rangle_{23}$ ,  $|\uparrow\downarrow\rangle_{23}$ , and  $|\uparrow\uparrow\rangle_{23}$ , we can observe clear four peaks in real part implying the four Bell states:

$$\begin{aligned} |\Phi^+\rangle_{14} &= \frac{1}{\sqrt{2}} (|\downarrow\downarrow\rangle_{14} + |\uparrow\uparrow\rangle_{14}), & |\Phi^-\rangle_{14} &= \frac{1}{\sqrt{2}} (|\downarrow\downarrow\rangle_{14} - |\uparrow\uparrow\rangle_{14}), \\ |\Psi^+\rangle_{14} &= \frac{1}{\sqrt{2}} (|\downarrow\uparrow\rangle_{14} + |\uparrow\downarrow\rangle_{14}), & |\Psi^-\rangle_{14} &= \frac{1}{\sqrt{2}} (|\downarrow\uparrow\rangle_{14} - |\uparrow\downarrow\rangle_{14}), \end{aligned} \quad (1)$$

**(a) Entanglement swapping circuit**



**(b) Bell state**



**(c) Two-qubit output density matrix after entanglement swapping circuit**

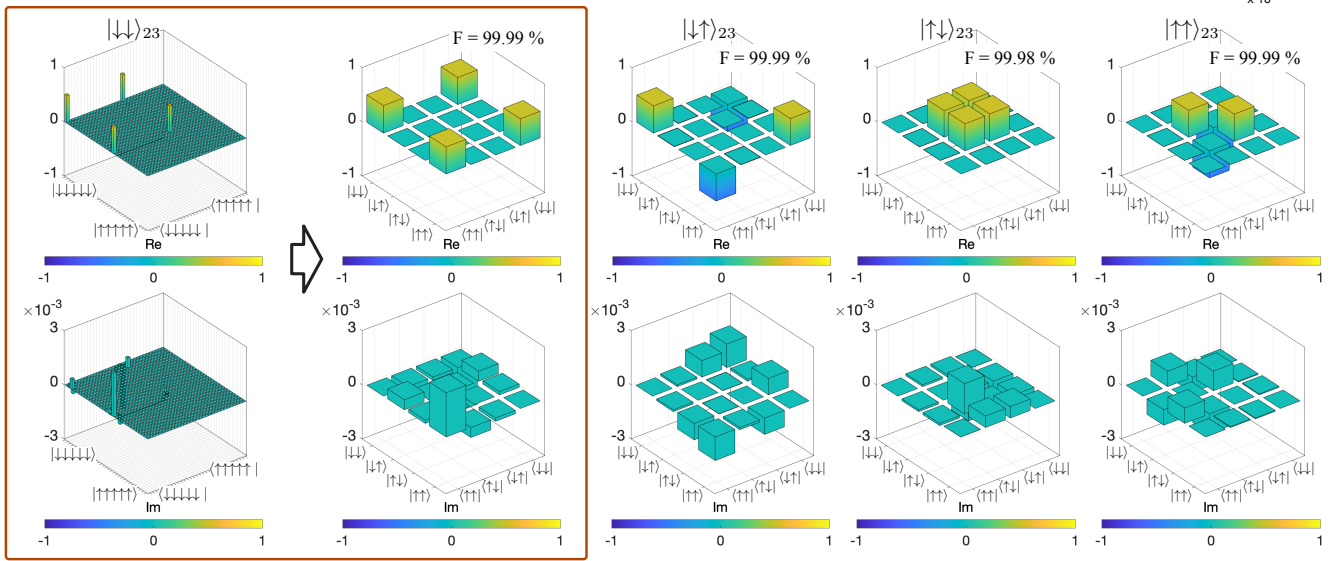
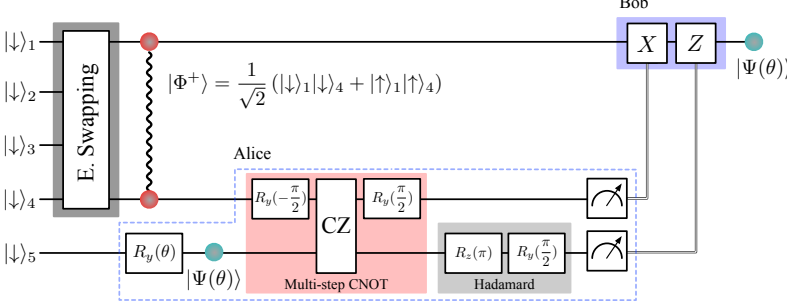


**Figure 5.** (a) Quantum circuit for implementing the entanglement swapping protocol. The subfigure in bottom of (a) shows the each gate operation time. Generation of the two Bell pairs is completed in 365.5 ns and the swapping protocol is completed in 541.0 ns (not including the operation time of the measurements). (b) At the step (i) of the process, two Bell pairs are created for (QD1, QD2) and (QD3, QD4), and its density matrix is shown in (b). The state fidelity of two Bell pairs is achieved about 99.99%. (c) The density matrices of the entangled two-qubit states at the final step, depending on the measurement outcomes on QD2 and QD3. In our simulation, the measurement process is mimicked by employing the projection operator, thus in fact the output state is given by the five-qubit state. For the sake of simplicity, we pick out the nonzero components from the full density matrix as described in the red box in (c), which represent the components of the two-qubit entangled states.

All cases show the state fidelities about 99.9% and the entanglement swapping protocol is completed in 541.0 ns as shown in the subfigure of Fig. 5(a), where the time for the measurements is not considered. Therefore, the entanglement swapping protocol is implemented successfully in our FQD system. The output entangled states will be used as the quantum channel in the quantum teleportation, which will be explained in the next section.

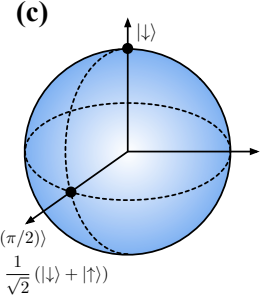
For the quantum teleportation process, the sender (Alice) and the receiver (Bob) need to share the entangled state as the quantum channel. In the previous section, we demonstrate the entanglement swapping protocol to create the Bell entangled state for the remote QD1 and QD4. Given the entangled state as the quantum channel, the quantum information can be sent

(a) Quantum teleportation circuit



(b)

Alice's outcome	Bob's unitary gate
$ \downarrow\downarrow\rangle_{45}$	Id
$ \downarrow\uparrow\rangle_{45}$	X
$ \uparrow\downarrow\rangle_{45}$	Z
$ \uparrow\uparrow\rangle_{45}$	XZ



(d) Bob's output density matrix

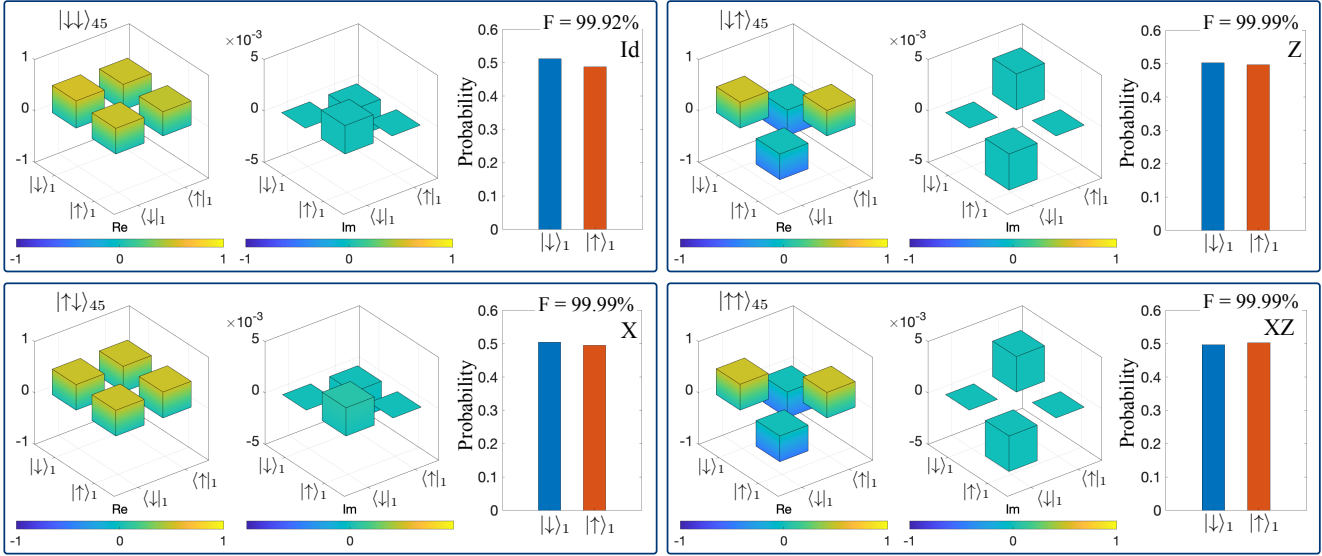


**Figure 6.** (a) Quantum teleportation circuit involving the entanglement swapping process that create the Bell entangled state to be used as a quantum channel in the teleportation process. Alice prepares an arbitrary state on QD5 and performs the Bell measurement on the spin-qubit in QD4 and QD5. Depending on the measurement outcomes by Alice, Bob's local operation is determined, which is summarized in (b). We test the validity of our simulation by employing an equal superposition of spin-up and down qubit as shown in (c). (d) The density matrices of Bob's output states before the local unitary gate (denoted by the purple color in (a)) and the probabilities obtaining the spin-up and -down states after the unitary gate depending on Alice's measurement outcomes.

from Alice to Bob. In our FQD system, the quantum information to be sent is encoded in the spin-qubit state on QD5. The quantum circuit of the teleportation is shown in Fig. 6(a). The initialized spin-down states are manipulated by the entanglement swapping operation, which creates the Bell entangled state between QD1 and QD4. In particular, we set the swapping circuit to create the output Bell entangled state as  $|\Phi^+\rangle_{14}$ . Note that the spin-qubit state of QD5 remains unchanged. Next, Alice prepare a quantum state to be teleported by mean of conducting the  $R_y(\theta)$  gate operation on the spin-qubit of QD5, which can generate an arbitrary superposition of the spin-up and -down qubit given by  $|\Psi(\theta)\rangle_5 = \cos(\theta)|\downarrow\rangle_5 + \sin(\theta)|\uparrow\rangle_5$ . For implementation of the teleportation, we first set  $\theta = \pi/2$  where the following state is prepared:  $|\Psi(\pi/2)\rangle_5 = (|\downarrow\rangle_5 + |\uparrow\rangle_5)/\sqrt{2}$ . Then, Alice performs the Bell measurement on the two spin-qubit on QD4 and QD5, where one of them is obtained from the Bell pair of the quantum channel and the other from the state to be teleported. As demonstrated in the previous section, we simulate the Bell measurement by conducting the multi-step CNOT and Hadamard gates sequentially, which are followed by the measurements. From the spin-up and -down bases measurements on QD4 and QD5 by Alice, four possible outcomes can be obtained. Then, Bob applies the appropriate local operations depending on the measurement outcomes from Alice side, summarized in Fig. 6(b), to the spin-qubit in his side (QD1) that comes from the remaining spin-qubit of the entangled qubit on QD1. Finally, the spin-qubit state on QD1 can be transformed into the state that Alice would like to send. Figure 6(d) shows the output density matrices of the spin-qubit state on QD1 depending on the measurement outcomes of QD4 and QD5. Additionally, the bar graph



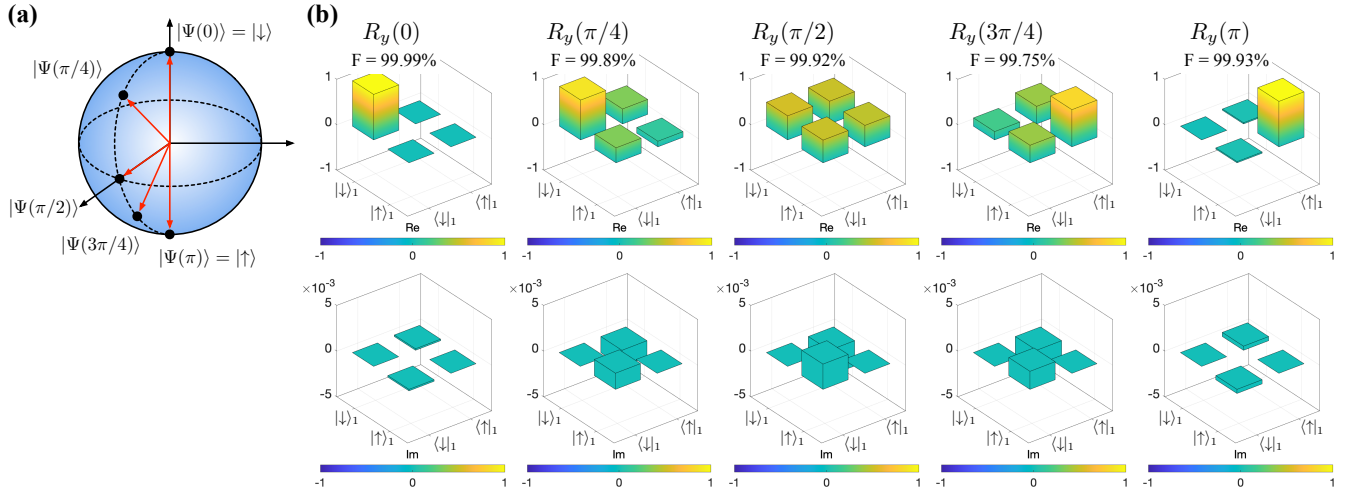


**Figure 7.** Quantum teleportation for arbitrary superposition spin-qubit. (a) Our working examples are depicted in the Bloch sphere and (b) the density matrices of the corresponding teleported states. Our simulation results are obtained with the assumption of the Alice’s measurement outcomes as  $|\downarrow\downarrow\rangle_{45}$ .

shown on the right side each density matrix represents the probability of spin-up and -down state on QD1, i.e., the output state that Bob applies the local operation based on the Alice’s measurement outcome. It must be equal to the state that Alice would like to send if the quantum teleportation works well. All results show the state fidelities between the teleported states and the desired states are around 99.9%. We also simulate the teleportation of the arbitrary angle of  $R_y(\theta)$ , in which the input state to be teleported is give by  $|\Psi(\theta)\rangle_5 = \cos(\theta)|\downarrow\rangle_5 + \sin(\theta)|\uparrow\rangle_5$ . In particular, we test five examples of  $\theta = (0, \frac{\pi}{4}, \frac{\pi}{2}, \frac{3\pi}{4}, \pi)$  and the density matrix of each case is depicted in Fig. 7(b). For the sake of simplicity, Alice’s measurement outcome in the teleportation process is set to  $|\downarrow\downarrow\rangle_{45}$ . As shown in Fig. 7(b), the state fidelities for all cases are reached between 99.75% and 99.99%, which indicate that our device simulation of the teleportation works well.

## Conclusion

Entanglement-based quantum information applications defined in the electrode-driven Silicon five quantum dot (FQD) platform are computationally investigated, where qubits are encoded in the confined electron spins. We elaborately explore the device design of our FQD system by employing an in-house simulations which integrate the bulk physics and the empirical representation of electronic structure. The DC control biases capable of the spin qubits initialization are calculated with rigorous simulations of the FQD structure, which allow to implement the native logic gate operations. Given the gate biases, we first demonstrate the individual 1-qubit rotation and 2-qubit entangling logic gate operations, where we employ the multi-step CNOT gate for the entangling logic. Similarly to the previous modeling results<sup>9,10</sup>, the middle gate biases are solely fine-tuned to control the strength of the exchange interactions  $J$ . However, it is inadequate to adjust the single middle gate bias for controlling  $J$ , instead the other middle gate biases also need to fine-tune to change the strength the target  $J$ . Based on the results, the programmability of our FQD system are verified by implementing three quantum information applications such as the generation of the magic states, the entanglement swapping protocol, and the quantum teleportation. The magic state creation is carried in the regime of the weak interaction, but the other applications in the regime of the strong interaction due to the entangling gating operations. As a result, we show that the electron spin qubits on QD1 and QD4 are entangled by implementing the entanglement swapping, where the two qubits on QD1 and QD4 have never been interacted during the process. The state fidelities are reached over 99.9%. Finally, we examine the quantum teleportation protocol with several arbitrary superposition states, where the final entangled state from the entanglement swapping is incorporated in the quantum channel in the teleportation process. The state fidelities of the cases we simulate are almost over 99.8%. Although we have not investigated the noise effects of our simulation, the results in this work can be served as a solid case study showing the extended capability of our simulation-driven design method compared to previous studies<sup>9-11</sup>.

## Acknowledgements

This work is supported by the National Research Foundation of Korea grant (NRF-2022M3E4A1072893) funded by the Korea government (MSIT).

## References

1. Kobayashi, T. *et al.* Engineering long spin coherence times of spin–orbit qubits in silicon. *Nat. Mater.* **20**, 38–42 (2021).
2. Muhonen, J. T. *et al.* Storing quantum information for 30 seconds in a nanoelectronic device. *Nat. nanotechnology* **9**, 986–991 (2014).
3. Veldhorst, M. *et al.* An addressable quantum dot qubit with fault-tolerant control-fidelity. *Nat. nanotechnology* **9**, 981–985 (2014).
4. Kawakami, E. *et al.* Gate fidelity and coherence of an electron spin in an Si/SiGe quantum dot with micromagnet. *Proc. Natl. Acad. Sci.* **113**, 11738–11743 (2016).
5. Bertrand, B. *et al.* Fast spin information transfer between distant quantum dots using individual electrons. *Nat. nanotechnology* **11**, 672–676 (2016).
6. Zajac, D. M. *et al.* Resonantly driven cnot gate for electron spins. *Science* **359**, 439–442 (2018).
7. Takeda, K. *et al.* Quantum tomography of an entangled three-qubit state in silicon. *Nat. Nanotechnol.* **16**, 965–969 (2021).
8. Philips, S. G. *et al.* Universal control of a six-qubit quantum processor in silicon. *Nature* **609**, 919–924 (2022).
9. Kang, J.-H. & Ryu, H. Quantum information processing in electrically defined silicon triple quantum dot systems. *Solid-State Electron.* **213**, 108863 (2024).
10. Ryu, H. & Kang, J.-H. Devitalizing noise-driven instability of entangling logic in silicon devices with bias controls. *Sci. Reports* **12**, 15200 (2022).
11. Kang, J.-H., Ryu, J. & Ryu, H. Exploring the behaviors of electrode-driven si quantum dot systems: from charge control to qubit operations. *Nanoscale* **13**, 332–339 (2021).
12. Kawakami, E. *et al.* Electrical control of a long-lived spin qubit in a Si/SiGe quantum dot. *Nat. nanotechnology* **9**, 666–670 (2014).
13. Takeda, K. *et al.* A fault-tolerant addressable spin qubit in a natural silicon quantum dot. *Sci. advances* **2**, e1600694 (2016).
14. Yoneda, J. *et al.* A quantum-dot spin qubit with coherence limited by charge noise and fidelity higher than 99.9%. *Nat. nanotechnology* **13**, 102–106 (2018).
15. Huang, W. *et al.* Fidelity benchmarks for two-qubit gates in silicon. *Nature* **569**, 532–536 (2019).
16. Xue, X. *et al.* Quantum logic with spin qubits crossing the surface code threshold. *Nature* **601**, 343–347 (2022).
17. Mađzik, M. T. *et al.* Precision tomography of a three-qubit donor quantum processor in silicon. *Nature* **601**, 348–353 (2022).
18. Noiri, A. *et al.* Fast universal quantum gate above the fault-tolerance threshold in silicon. *Nature* **601**, 338–342 (2022).
19. Watson, T. *et al.* A programmable two-qubit quantum processor in silicon. *nature* **555**, 633–637 (2018).
20. Takeda, K., Noiri, A., Nakajima, T., Kobayashi, T. & Tarucha, S. Quantum error correction with silicon spin qubits. *Nature* **608**, 682–686 (2022).
21. Howard, M., Wallman, J., Veitch, V. & Emerson, J. Contextuality supplies the ‘magic’ for quantum computation. *Nature* **510**, 351–355 (2014).
22. Oliviero, S. F., Leone, L., Hamma, A. & Lloyd, S. Measuring magic on a quantum processor. *npj Quantum Inf.* **8**, 148 (2022).
23. Żukowski, M., Zeilinger, A., Horne, M. A. & Ekert, A. K. ‘‘Event-ready-detectors’’ Bell experiment via entanglement swapping. *Phys. Rev. Lett.* **71**, 4287 (1993).
24. Bose, S., Vedral, V. & Knight, P. L. Multipartite generalization of entanglement swapping. *Phys. Rev. A* **57**, 822 (1998).
25. Dür, W., Briegel, H.-J., Cirac, J. I. & Zoller, P. Quantum repeaters based on entanglement purification. *Phys. Rev. A* **59**, 169 (1999).